# An Electrochemical Biochip for Measuring Low Concentrations of Analytes With Adjustable Temporal Resolutions

Kae-Dyi You, *Student Member, IEEE*, Edoardo Cuniberto, Shao-Cheng Hsu, Bohan Wu, *Student Member, IEEE*, Zhujun Huang, Xiaochang Pei, and Davood Shahrjerdi, *Senior Member, IEEE*

***Abstract*—Electrochemical micro-sensors made of nano-graphitic (NG) carbon materials could offer high sensitivity and support voltammetry measurements at vastly different temporal resolutions. Here, we implement a configurable CMOS biochip for measuring low concentrations of bio-analytes by leveraging these advantageous features of NG micro-sensors. In particular, the core of the biochip is a discrete-time $\Delta\Sigma$ modulator, which can be configured for optimal power consumption according to the temporal resolution requirements of the sensing experiments while providing a required precision of $\approx$13 effective number of bits. We achieve this new functionality by developing a design methodology using the physical models of transistors, which allows the operating region of the modulator to be switched on-demand between weak and strong inversion. We show the application of this configurable biochip through *in-vitro* measurements of dopamine with concentrations as low as 50 nM and 200 nM at temporal resolutions of 100 ms and 10 s, respectively.**

***Index Terms*—Biochip, electrochemical sensing, lab-on-a-chip, system-on-a-chip, voltammetry.**

## I. Introduction

ELECTROCHEMICAL sensors are used widely in sensing experiments due to their ease of fabrication, simple operation, and applicability for the detection of many electroactive molecules [1]. Recording the output of these sensors requires a detection circuitry that performs amplification and digitization of the signal. The combination of the sensor and the detection circuitry forms an electrochemical sensing unit. Miniaturization of the sensing unit has been an important research direction because it allows packing these units into a dense array, resulting in an electrochemical biochip [2]–[9]. As a result, this family of biochips could perform many parallel measurements, making them an attractive choice for a wide range of applications from fundamental studies of chemical signaling in living cells [7] to point-of-care (PoC) diagnostics [8].

The use of complementary metal-oxide-semiconductor (CMOS) technology for building the detection circuitry has been central to advancing the capabilities of electrochemical biochips. In particular, CMOS technology has enabled the realization of various system-on-a-chip (SoC) concepts in electrochemical sensing [2]–[8], [10]–[14]. Compared to their counterparts made of commercial off-the-shelf (COTS) components, these SoCs have a smaller footprint, consume less power, and provide better performance. Two main reasons underlie this progress. The first reason is the ability of the CMOS technology to integrate many transistors reliably on the same substrate, resulting in advanced integrated circuits (ICs). The second reason is the existence of a well-established CMOS ecosystem, from the design tools to the foundry services, which has allowed the efficient implementation of custom-made SoCs. This capability is particularly vital for utilizing the benefits arising from the continuing advances of electrochemical sensors and measurement techniques.

Of various advances, development of micro-fabricated sensors from carbon materials (for example see Ref. [15]–[20]) promises biochips with new experimental capabilities. In particular, micro-fabricated sensors could support cyclic voltammetry experiments with a wide range of potential sweep rates, due to their small RC time constant [1]. This property enables a user to adjust the temporal resolution of the measurements according to the needs of the sensing experiments. As we explain later, this can be achieved through a proper engineering of the voltammetry waveform. A biochip with an adjustable temporal resolution will be particularly useful for making measurements in complex biological environments where bio-analytes could have different temporal dynamics.

A prime example of such an environment is the brain, where the changes of dopamine concentration, depending on its function, occur at two different temporal dynamics: tonic and phasic (e.g., see Refs. [21]–[23]). The tonic mode represents the extracellular level of the baseline dopamine that changes slowly over minutes to hours. In contrast, the extracellular dopamine level in the phasic mode changes rapidly, on the order of seconds. Importantly, the physiological levels of interest for phasic and tonic dopamine are remarkably low— generally on the order of

Manuscript received April 6, 2020; revised June 12, 2020; accepted July 8, 2020. Date of publication July 14, 2020; date of current version August 17, 2020. The work was supported in part by NSF under Awards 1728051 and 1940764, in part by the instrumentation grants from NSF under Grant MRI-1531664, and in part by Gordon and Betty Moore Foundation under Grant GBMF 4838 This article was recommended by Associate Editor Prof. Pedram Mohseni. *(Corresponding author: Davood Shahrjerdi.)*

The authors are with the Department of Electrical and Computer Engineering, New York University, Brooklyn, NY 11201 USA (e-mail: kd.you@nyu.edu; edocuni@nyu.edu; sch474@nyu.edu; bw1417@nyu.edu; zhujun@nyu.edu; xiaochangpei@nyu.edu; davood@nyu.edu).

Color versions of one or more of the figures in this article are available online at https://ieeexplore.ieee.org.

Digital Object Identifier 10.1109/TBCAS.2020.3009303

10 nM [24], [25] and 100 nM, respectively [26]–[28]. As a result, measuring such low concentrations is highly demanding. While the high sensitivity of sensors made of carbon nanomaterials is useful for improving the limit of detection [20], [29], measuring such low concentrations will only be possible when these sensors are complemented with high-precision detection ICs.

Here, we show how the design of the sensor and the detection IC together can result in an optimum performance. We describe the systematic implementation of a high-precision detection IC around the specifications of high-sensitivity micro-sensors made of NG carbon—a form of carbon nanomaterial—that our lab is developing for voltammetry sensing applications [17], [20]. To provide an optimal power consumption, the detection IC adapts its operating mode to the temporal resolution of the measurements without the loss of precision. We demonstrate *in-vitro* measurements of low-concentration dopamine with temporal resolutions of 100 ms and 10 s.

Section II briefly discusses the requirements for the detection of bio-analytes at low concentrations in voltammetry measurements. Section III focuses on the design and implementation of the detection IC affording both high-precision and configurable operating modes. Section IV provides the *in-vitro* cyclic voltammetry measurements of dopamine.

## II. System Specifications

### A. Sensing Bio-Analytes Using Voltammetry

We used the voltammetry technique for implementing our sensing system. A basic overview of this technique is useful for describing our approach to designing the system. Voltammetry is an electrochemical sensing technique, which applies a varying potential to the sensor and measures the resulting currents [1]. Of various approaches, cyclic voltammetry employing a linear sweep of the potential in time (e.g., see Fig. 1(a)) has been highly popular for two main reasons. The first reason is the ease of constructing cyclic voltammograms (i.e., plotting the redox current against the applied potential as shown in Fig. 1(d)) from the measured time-varying data. These plots are useful for identifying an analyte of interest using its redox potential fingerprints. The second reason is the ability to readily adjust the temporal resolution of the measurements by varying the repetition rate of the potential waveform. The operating mechanism of the sensor (i.e., diffusion-controlled or adsorption-controlled) plays a critical role in optimizing the voltammetry time ($t_{cv}$) and the delay time ($t_d$) of the potential waveform (see Fig. 1(a)).

However, a shortcoming of this voltammetry technique is the background current signal generation, as shown in Fig. 1(b). Two sources contribute to the background current. The first one is the charge and discharge of the sensor capacitance in an ionic solution, the blue curve denoted as $I_{cap}$ in Fig. 1(b). Pseudocapacitance is the other source, which is due to the electrochemical interactions of a redox-active species on the sensor surface with the ionic solution. For example, the interactions of quinone-like species on carbon sensors with cations generate additional background currents, which occur at low potentials (generally around 0 V; see the green curves denoted as $I_{quinone}$ in Fig. 1(b) [30].

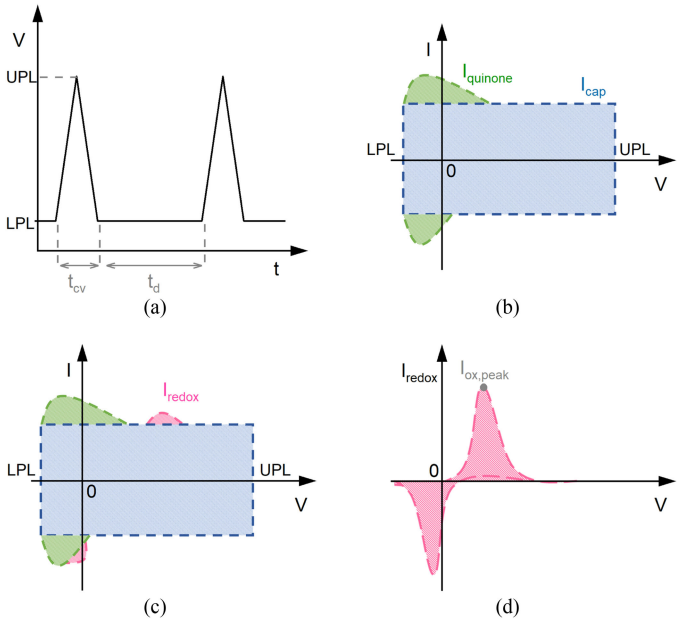


Fig. 1. (a) Schematic illustration of a triangular potential waveform. The potential is varied linearly in time between a lower potential limit (LPL) and an upper potential limit (UPL).The potential sweep rate is 2(UPL-LPL)/$t_{cv}$. (b) An illustration showing the current-voltage (I-V) characteristics of the background signal. (c) The addition of a target bio-analyte to the solution generates a redox current ($I_{redox}$). (d) Cyclic voltammogram obtained by subtracting the background signal, panel (b), from the total signal, panel (c).

When a target bio-analyte is in the solution, the sensor produces a redox current ($I_{redox}$), as shown in Fig. 1(c). The magnitude of the background signal is noticeably larger than this redox current (i.e., the signal of interest). Critically, measuring a large background signal generally trades off with the digitization precision due to limitations in increasing the number of digitization bits. This is an undesirable constraint because the digitization error generally dominates the noise of the measurements in voltammetry experiments, imposing a limit on the lowest measurable concentration. Therefore, as the amplitude of the background current relative to the redox current increases, the trade-off between the input current range and the noise of the measurements becomes more severe [8], [31], [32]. As we explain below, this limitation is a more significant challenge for measuring low concentrations of bio-analytes in experiments employing waveforms with a rapid potential sweep (RPS) than those with a slow potential sweep (SPS). Therefore, we began the design of the detection IC around the characteristics of our NG micro-sensors for RPS measurement of dopamine (see Section III-C).

### B. Sensor Characteristics Under SPS and RPS

To better illustrate the rationale behind our design strategy, let us briefly discuss how scaling the potential sweep rate influences the amplitude of both the redox and the background currents in cyclic voltammetry measurements. We define the scaling factor as the ratio of a potential sweep rate to an arbitrary reference sweep rate under the same operating regime of the sensor (i.e.,

TABLE I
EFFECT OF POTENTIAL SWEEP RATE SCALING ON SENSOR PERFORMANCE IN SPS AND RPS MEASUREMENTS

| | SPS | RPS |
|---|---|---|
| Redox current peak ($I_{ox,peak}$) | $\propto K_{SPS}^{0.5}$ | $\propto K_{RPS}$ |
| Capacitive background current ($I_{cap}$) | $\propto K_{SPS}$ | $\propto K_{RPS}$ |
| SB ratio | $\propto K_{SPS}^{-0.5}$ | $\propto 1$ |

either RPS or SPS). Table I gives a summary of this scaling effect, where $K_{SPS}$ and $K_{RPS}$ denote the scaling factors under SPS and RPS, respectively.

In Fig. 1(b), the steady-state amplitude of $I_{cap}$ is given by $C_{sr} \times \nu$, where $C_{sr}$ and $\nu$ are the sensor capacitance and the potential sweep rate. In practice, $C_{sr}$ is not necessarily constant and depends on the frequency of the stimulation. More precisely, its frequency response is a mirrored s-shaped curve [33]—the sensor reaches its full capacitance only when the stimulation (e.g., potential sweep) is sufficiently slow. A small RC time constant is an essential factor for allowing the sensor to reach its full capacitance under high sweep rates. The high conductivity of graphitic materials contributes to a low resistance. The reduced capacitance of micro-sensors, due to their small area, further reduces the RC time constant. Therefore, for a wide range of potential sweep rates (from slow to rapid), a graphitic micro-sensor is expected to reach its full capacitance. As a result, the steady-state amplitude of $I_{cap}$ would increase linearly with the potential sweep rate.

Unlike $I_{cap}$, the peak of $I_{redox}$ (i.e., $I_{ox,peak}$ in Fig. 1(d)), varies in proportion with $\sqrt{K_{SPS}}$ in SPS experiments, where the redox reaction on the sensor surface is diffusion-controlled [1]. Because of this operating mechanism of electrochemical sensors, the incorporation of a delay time into the waveform in SPS measurements is unnecessary (i.e., $t_d = 0$ in Fig. 1(a)). This means that the temporal resolution of the SPS measurements is adjusted by varying the potential sweep rate. Therefore, reducing the temporal resolution (i.e., by reducing $K_{SPS}$) decreases the amplitude of $I_{cap}$ at a higher rate than $I_{ox,peak}$. As a result, in experiments requiring low temporal resolutions, the potential sweep rate can be used as an additional knob for increasing the ratio of the redox signal peak relative to the capacitive portion of the background signal. We call this sensor performance metric measured in response to 1 $\mu$M of a bio-analyte as the SB ratio and define it as: SB ratio $\triangleq I_{ox,peak}/I_{cap}$. This property of SPS is favorable for relaxing the trade-off between the input current range and the digitization error of the detection IC.

In RPS measurements, however, the redox reaction is adsorption-limited [1]. In this operating regime, the voltammetry time ($t_{cv}$) is much shorter than the diffusion time of bio-analytes from the bulk of the solution to the sensor surface. Hence, $I_{redox}$ in RPS measurements is shaped by the concentration of adsorbed bio-analytes ($[A]_{adsorb}$) on the sensor surface. To increase $[A]_{adsorb}$, the potential waveform in RPS measurements generally includes a delay time ($t_d$), which is noticeably longer than $t_{cv}$. While increasing $t_d$ increases $I_{ox,peak}$, it compromises the temporal resolution (i.e., $t_{cv} + t_d$). For a given $t_d$, however, $I_{ox,peak}$ varies linearly with $K_{RPS}$, causing its ratio relative to $I_{cap}$ to remain unchanged.

From the above discussions, $I_{cap}$ is much larger in RPS than SPS due to higher sweep rates. Further, the SB ratio is typically smaller in RPS than SPS due to their differences in $I_{ox,peak}$ dependence on the potential sweep rate. Therefore, the digitization error of the detection IC is expected to be more critical for detecting low concentrations of bio-analytes in RPS than SPS.

One existing approach for alleviating this difficulty of RPS has been to first record the background signal prior to the experiments, then average it to reduce the noise, and finally subtract the averaged background from the measured current in real-time. The underlying assumption of this technique, known as the analog background subtraction [31], is that the background signal is time-invariant, or else its changes are predictable and can be modeled. In practice, however, the amplitude of the background current experiences a noticeable drift, and the variation of its amplitude, even at a given potential, is unpredictable. More critically, the variations of the background current amplitude are generally non-uniform at different potentials in a given measurement cycle, resulting in the distortion of the shape of the background signal [31], [34]. These complications could limit the reliability of data analysis, particularly in the presence of interferes [34]–[36]. Hence, an optimum solution for measuring low concentrations of bio-analytes under RPS conditions is to record the full shape of the background signal with high precision and use it for data analysis (see recent examples in Refs. [37], [38]).

### C. NG Micro-Sensor Implementation

For implementing micron-sized electrochemical sensors, we employed planar NG carbon materials. The rationale for choosing NG carbon is the fast electron transfer property of graphitic materials [19], which is highly useful for achieving a high redox current in electrochemical sensing measurements [1]. There is a consensus that the electrochemical properties of carbon nanomaterials (i.e., redox current and capacitance) strongly depend on their material structure (e.g., see Refs. [19], [39]). In a recent study, we have provided empirical models for nano-engineering the structure of NG carbon materials in order to optimize their electrochemical properties [20]. We found that the average density of point defects ($n_{0D}$) in NG carbon is the dominant factor in shaping the redox current in RPS measurements of dopamine. Further, we showed that the average graphitic crystallite size ($L_a^2$) and $n_{0D}$, for the range of defects studied, can predict the capacitance of NG carbon. Overall, the findings of our recent study indicate that the SB ratio of NG carbon can be enhanced by simultaneously increasing $L_a^2$ and $n_{0D}$ during the material synthesis.

In this study, we aimed to produce NG micro-sensors with $L_a^2 \approx 1000 \pm 100$ nm$^2$ and $n_{0D} \approx 8$–$9 \times 10^{11}$ cm$^2$. For these defect densities, our empirical capacitance model predicts an area-normalized capacitance of $\approx$ 90–100 $\mu$F/cm$^2$. Also, from our experimental observations of NG carbon with these defect densities, we expect an SB ratio of $\geq$0.25 and $\geq$0.5 nA/($\mu$M

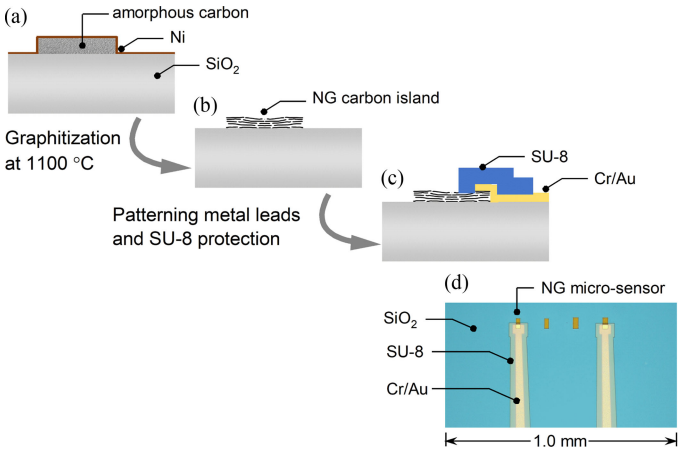


Fig. 2. (a)–(c) Main fabrication steps of the NG micro-sensors. (d) Optical image of a sensor sample.

· nA) for measuring dopamine under RPS (200 V/s) and SPS (0.1 V/s) conditions. Lastly, for these NG micro-sensors, the amplitude of $I_{quinone}$ is typically comparable to $I_{cap}$.

We have provided a detailed description of the NG carbon material synthesis and micro-sensor fabrication in Ref. [20]. The target structural properties of the NG carbon were achieved by using a sub-1 nm nickel catalyst for the material synthesis. Fig. 2(a)–c illustrates the main steps of the material production and sensor fabrication process. In brief, the first step involves the deposition of the nickel catalyst under ultra-high vacuum (UHV) onto lithographically defined amorphous carbon islands. Next, these islands were converted into an NG carbon material through annealing at 1100 °C in an $Ar/H_2$ ambient. The NG carbon islands were then made into functional devices by making Cr/Au metal contacts and forming insulating SU-8 protection layers using standard nano-fabrication techniques. Fig. 2(d) shows the optical image of fully-fabricated NG micro-sensors.

### D. Design Concept

To utilize the high redox current of our NG micro-sensors for measuring low concentrations of bio-analytes, they must be paired with a high-precision detection IC. Further, the circuit must be capable of measuring the full background current. Due to their micron-sized dimensions, our NG sensors can operate under a wide range of potential sweep rates, from a few mV/s to >100 V/s. We take advantage of this feature to configure the operating region of our detection IC for an optimal power consumption according to the temporal resolution requirements of the sensing experiment. Specifically, our detection IC operates in weak inversion for experiments employing SPS, where a temporal resolution of a few seconds is adequate. To accommodate high temporal resolution measurements using RPS, we switch the operating region of the IC to strong inversion. The key to achieving this configurable feature is an analytical framework for the design of a class-AB opamp, which builds on the physical models of transistors in weak and strong inversion regions. We use this opamp to implement a high-precision discrete-time (DT) $\Delta\Sigma$ modulator.

TABLE II
SYSTEM SPECIFICATIONS FOR MEASURING PHASIC AND TONIC DOPAMINE USING NG MICRO-SENSORS

| Parameter | SPS | RPS |
|---|---|---|
| Minimum [DA] (nM) | 100 | 10 |
| Temporal resolution (s) | 10 | 0.1 |
| Sensor capacitance ($\mu$F/cm$^2$) | ≈110-125* | ≈90-100 |
| SB ratio (nA.$\mu$M$^{-1}$.nA$^{-1}$) | $\gtrsim$ 0.5 | $\gtrsim$ 0.25 |
| Potential sweep rate (V/s) | 0.1 | 200 |
| LPL, UPL (V) | -0.1, 0.4 | -0.2, 0.6 |
| $t_d$ (ms) | 0 | 92 |
| $I_{cap}$†(nA) | $\lesssim 80\times10^{-3}$ | $\lesssim$ 125 |
| $I_{quinone}$ (nA) | $\lesssim 80\times10^{-3}$ | $\lesssim$ 125 |
| $\overline{I_{noise}}$ (pA$_{rms}$) | $\lesssim$ 0.4 | $\lesssim$ 32 |

*We assumed an approximate 25% extra capacitance for SPS because of the frequency dependence of the capacitance.
†We assumed a maximum sensor area of 625 $\mu$m$^2$.

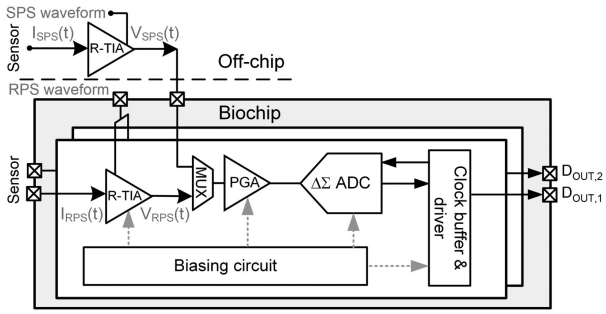


Fig. 3. System architecture of our prototype detection IC, consisting of 2 independent measuring channels.

Table II lists the system-level specifications for measuring low concentrations of dopamine under two specific SPS and RPS waveforms, which are nearly optimal for operating our NG micro-sensors. Further, we generally build sensors with a geometric area smaller than 625 $\mu$m$^2$. Lastly, we estimated the noise requirements for detecting 10 and 100 nM of dopamine under RPS and SPS by considering two factors. First, according to the Rose criterion, the minimum amplitude of a detectable current by the detection IC must be five times larger than the root-mean-square (rms) of the noise current. Second, the cyclic voltammogram is generated by subtracting the background current from the total current (see Fig. 1). Therefore, to generate a detectable cyclic voltammogram, the minimum $I_{ox,peak}$ must be at least ten times larger than the rms noise current ($\overline{I_{noise}}$). We used the specifications in Table II as the basis for implementing the detection IC.

## III. IMPLEMENTATION OF DETECTION IC

### A. System Architecture

Fig. 3 shows the system architecture of our prototype detection IC consisting of a front-end amplifier circuit, a programmable gain amplifier (PGA), followed by an analog-to-digital converter (ADC). This architecture, due

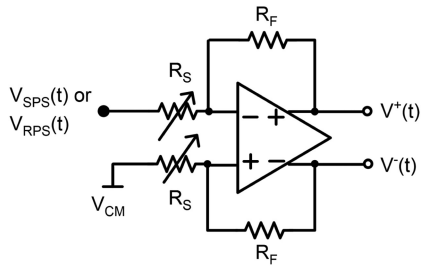


Fig. 4. Schematic illustration of the PGA. This circuit rejects the common-mode noise and provides up to 6 dB of amplification gain.

to its ease of implementation, has been popular in voltammetry experiments [1], [40].

The first amplifier stage performs two functions. It converts the input current to an output voltage and simultaneously amplifies the input signal. There are different ways of implementing the first stage including resistive-feedback transimpedance amplifier (R-TIA) circuits [7], current mirror circuits [14], and capacitive-feedback TIA (C-TIA) circuits [9]–[11]. However, the choice of the amplifier architecture has little bearing on the objective of our study here, which is to implement a configurable ADC. Therefore, we used R-TIA circuits in our study due to their simplicity. We chose the amplification gain of the R-TIA (i.e., the value of the feedback resistor, $R_{fb}$) such that the noise of R-TIA should not become a limiting factor in measuring the lowest redox current in our *in-vitro* measurements. In particular, we chose $R_{fb}$ values of 4 GΩ and 4.1 MΩ for the SPS and RPS experiments, respectively. With these choices, our detection IC supports an input current range up to ±350 nA (pA) in RPS (SPS). The consideration for accommodating a higher input current than what is listed in Table II is to provide flexibility for performing future experiments that may involve micro-sensors with a higher capacitance, micro-sensors with a larger area, or voltammetry using higher potential sweep rates. Given its reasonably small resistance value, the R-TIA circuit for RPS measurements was implemented on-chip in this prototype detection IC. However, it is not feasible to implement an on-chip R-TIA for the SPS measurements, due to its large resistor requirement. Instead, for a proof-of-concept demonstration, we used an off-chip R-TIA amplifier (SR570, Stanford Research Systems).

A PGA circuit follows the R-TIA circuits. We used a differential subtractor circuit for implementing the PGA. Fig. 4 shows the schematic of this PGA circuit. One function of the PGA here is to convert the single-ended voltage signal at its input into a differential one at its output. This conversion is beneficial for enhancing the robustness of the signal to various sources of common-mode noise, including interference from the power supply and on-chip digital circuits. The PGA also amplifies the output of the R-TIA (gain factors of 0, +3, or +6 dB) so that its peak amplitude is comparable to the maximum input range of the ADC. This is to utilize fully the digitization capability of the ADC and is particularly beneficial when using small NG micro-sensors, for which the background signal is noticeably smaller than the input range of R-TIA.

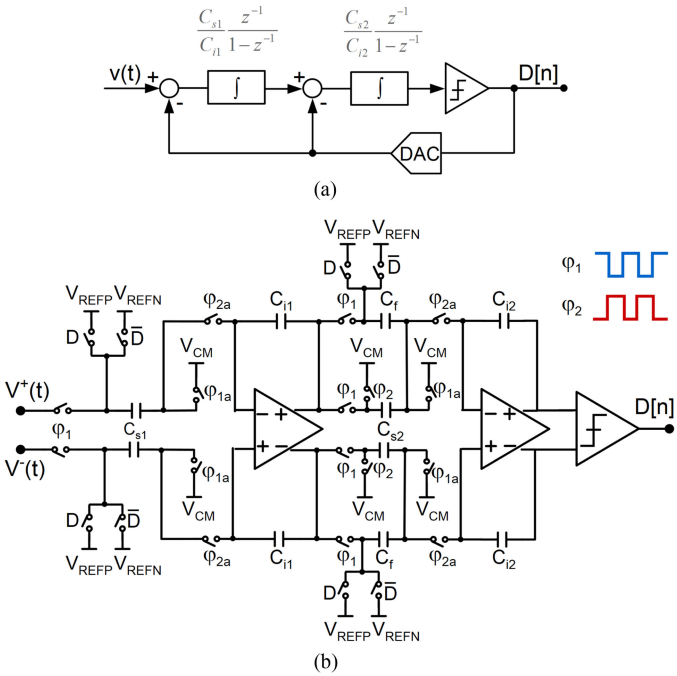


Fig. 5. (a) Block diagram of a second-order 1-bit ΔΣ ADC. (b) High-level circuit schematic of a DT second-order ΔΣ ADC. In our design, we used $C_{s1}/C_{i1} = 0.2$ and $C_{s2}/C_{i2} = 0.2$.

The output of the PGA is then quantized by a second-order DT ΔΣ modulator. Fig. 5 shows the block diagram and the high-level schematic of this ADC, consisting of two switched-capacitor integrators, a 1-bit quantizer (a Yukawa clocked comparator [41]), and a 1-bit DAC. The use of a 1-bit digital output is favorable for facilitating the digital readout of a biochip comprising many sensing units [8]. The output of the modulator is sent off-chip for processing (digital filtering and decimation) and data analysis.

### *B. ADC Implementation*

The rationale behind choosing a DT ΔΣ modulator is to realize a configurable ADC that adapts to the temporal resolution requirements of the voltammetry measurements without trading off its resolution. Let us elaborate on how this ADC architecture could achieve this objective.

The signal-to-noise and distortion ratio (SNDR) determines the resolution of an ADC. The peak SNDR of a 1-bit ΔΣ modulator, in the absence of non-idealities, is given by [42]

$$\mathrm{SNDR}_{peak} = 7.78 - 10 \times \log\left(\frac{\pi^{2N}}{2N+1}\right) + 10 \times (2N+1) \times \log(\mathrm{OSR}) \quad (1)$$

where N is the order of the ΔΣ modulator, and OSR is the oversampling ratio defined as the ratio of the oversampling clock frequency ($f_s$) to the output data rate of the decimation filter ($f_{DR}$). Due to the Nyquist criterion, the decimation filter generally outputs the data at a rate of $2f_b$, where $f_b$ is the signal bandwidth. Equation 1 illustrates that, for a given N, the peak

SNDR remains unchanged when scaling both $f_s$ and $f_b$ with the same factor. This is an important insight because the signal bandwidths under SPS and RPS are vastly different from each other. It ranges from tens of Hz in SPS measurements to a few kHz in RPS measurements. Therefore, for a given SNDR, the clock frequency of the $\Delta\Sigma$ modulator can ideally be 100 times smaller in SPS than in RPS measurements (assuming a $2f_b$ of 100 Hz and 10 kHz, respectively).

The ability of DT $\Delta\Sigma$ modulator to support the reduction of $f_s$ commensurate with $f_b$ during SPS measurements significantly relaxes the requirements of the opamps used in the loop filters. This presents an opportunity to implement an opamp that could provide optimal power consumption according to the temporal resolution requirement of the measurements. We introduce a framework for the design and implementation of such an opamp in Section III-D.

### C. SNDR Requirement of ADC

As we discussed in Section II, the ADC resolution is expected to become more critical in RPS than SPS measurements of dopamine. Hence, we used the RPS characteristics of our NG micro-sensors, listed in Table II, for determining the required ADC resolution. We simplified the calculations for finding the required ADC resolution by ignoring the noise contributions of R-TIA, PGA, and the sensor, hence attributing the measurement noise entirely to the quantization error of the ADC ($\overline{q_n}$). With this assumption, $\overline{q_n} = \overline{I_{noise}} \times R_{fb} \times A_{PGA}$. Using $\overline{I_{noise}}$ requirement for detecting 10 nM of dopamine in RPS measurements (see Table II), $R_{fb}$ of 4.1 M$\Omega$, and $A_{PGA} = 0$ dB, the estimated $\overline{q_n}$ is about 131 $\mu V_{rms}$. Hence, assuming an ADC with a rail-to-rail input range (supply voltage of $\pm$1.65 V), the effective number of bits (ENOB) must be 13 bits or better (i.e., SNDR $\geq$ 80 dB).

### D. Framework for Implementing a Configurable Opamp

For a second-order modulator with an OSR of 128, equation 1 predicts a peak SNDR of 97 dB. In practice, however, various sources of non-ideality degrade the ADC performance. Important examples include sampling jitter, thermal noise of switches, and opamp non-idealities. Behavioral modeling of the DT modulator is a critical step to estimate the effect of non-idealities on the ADC performance. To do so, we followed the modeling framework of Malcovati *et al.* [43] and developed the MATLAB SIMULINK model of a second-order DT modulator, which considers sampling jitter, thermal noise of switches (i.e., $k_B$T/C noise), and opamp non-idealities.

Next, we determined the opamp requirements under both the SPS ($2f_b$ = 100 Hz) and RPS ($2f_b$ = 10 kHz) measurement conditions. To do so, we performed parametric calculations in MATLAB by considering one source of opamp non-ideality at a time. In particular, we calculated SNDR by varying the DC gain, slew rate (SR), gain-bandwidth product (GBW), and saturation voltage ($V_{op,sat}$). In all simulations, we assumed an OSR of 128. Fig. 6 shows the summary of the simulation results, illustrating the opamp requirements to achieve an estimated SNDR $\geq$ 80 dB under the SPS and RPS conditions. In these plots, notice the

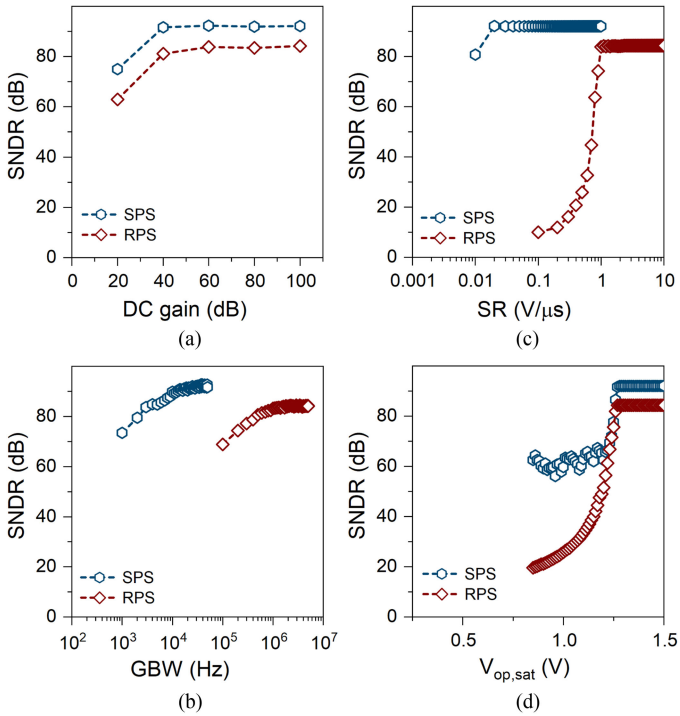


Fig. 6. Summary of opamp requirements for achieving SNDR $\geq$ 80 dB, assuming OSR = 128. Each plot was obtained by performing parametric behavioral simulations in MATLAB, considering one source of non-ideality at a time in DT modulator model.

remarkably relaxed requirements for GBW (Fig. 6(b)) and SR (Fig. 6(c)) under SPS conditions. We leverage this property for designing a configurable opamp, which allows switching of its operating region between strong and weak inversion regimes depending on the requirements of the voltammetry experiments (i.e., SPS *versus* RPS).

For implementing the $\Delta\Sigma$ modulator, we used a fully-differential two-stage opamp topology with a class-AB output stage. In Fig. 7, we show the transistor-level architecture of the opamp with a single-ended output, which is to simplify the opamp analysis. The reason for using a two-stage opamp is to allow a high open-loop gain for the physical implementation of the modulator, much larger than the minimum 60 dB requirement predicted by the behavioral simulations in Fig. 6(a). This practical consideration is important for reducing the integrator leakage, which otherwise contributes to the in-band noise of the integrator. The use of a class-AB guarantees a rail-to-rail signal swing at the output, hence fully removing the negative impact of opamp saturation voltage on SNDR. Further, the class-AB is capable of providing a high SR. This property is critical for suppressing harmonic distortion by avoiding a non-ideal transient response of the integrator during each sampling period [44]. These desirable features simplify the design process by focusing the required optimization on the opamp DC gain and bandwidth.

While this opamp topology has been used in the past [45], no formal framework exists for a configurable design of this opamp that allows its operation in both strong and weak inversion regimes. This can be achieved by identifying the key

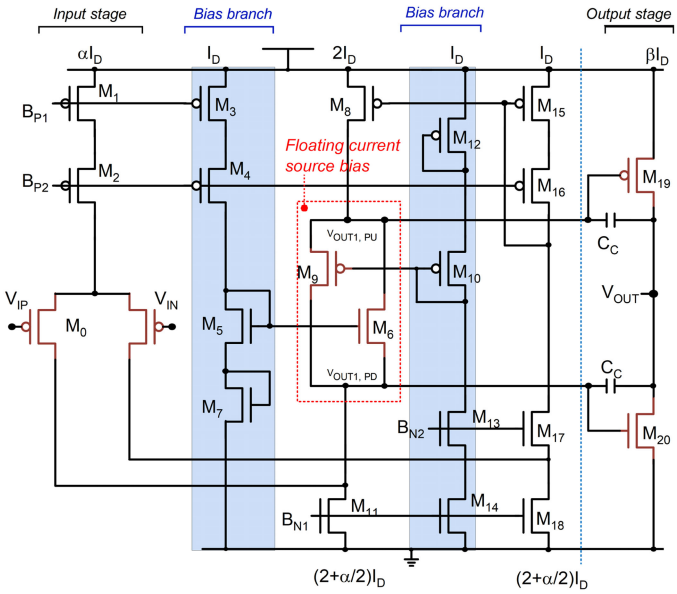


Fig. 7. Transistor-level schematic of the opamp with a class-AB output stage.

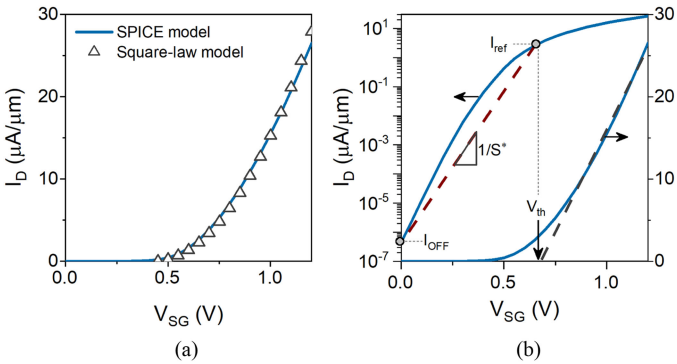


Fig. 8. (a) For the over-drive voltage range of interest, the square-law model fits the transfer characteristics well. (b) Extraction of the empirical model of the transistor current in weak inversion.

transistors that influence the performance of the opamp. Fig. 7 shows the main transistors that determine the DC gain ($A_0$) and GBW, marked in maroon color. The biasing current branches are highlighted with blue shadings. With this knowledge, $A_0$ and GBW are given by

$$A_0 \approx g_{m,0} \cdot [(g_{m,9} r_{o,9} r_{o,8}) || r_{o,0} || r_{o,11}] \cdot g_{m,20} \cdot (r_{o,19} || r_{o,20}) \quad (2)$$

$$\text{GBW} \approx \frac{g_{m,0}}{C_C} \quad (3)$$

where $C_C$ is the compensation capacitor; $g_m$ and $r_o$ denote the small-signal transconductance and output resistance of the corresponding transistors in Fig. 7.

We obtained the final forms of $A_0$ and GBW in each operating region (i.e., strong or weak inversion) by replacing $g_m$ and $r_o$ with their corresponding expressions obtained from the physical models of the n-type and p-type transistors. In Fig. 8, we show an example of data for the physical models, which we used for a p-type transistor. We used the square-law model for strong inversion. As shown in Fig. 8(a), the square-law model provides a good match for the range of $V_{SG}$ that the transistors operate in our design. Specifically, we targeted an over-drive voltage of $\approx$ 0.2 V in our design to allow better matching between transistors. For weak inversion, we derived an empirical model of the transfer characteristics of transistors following the procedure in Ref. [46]. Fig. 8(b) illustrates the details of this modeling approach. In short, we first determined the threshold voltage ($V_{th}$) by linear extrapolation, the drain current at $V_{th}$ ($I_{ref}$), the OFF current ($I_{OFF}$) at $V_{SG} = 0$ V, and the effective subthreshold swing ($S^*$). Based on this modeling procedure, the width-normalized transistor current in the weak inversion is given by

$$\frac{I_{sub}}{W} = I_{ref} 10^{\frac{(V_{SG} - |V_{th}|)}{S^*}} \quad (4)$$

This model relates the transistor current to the design parameters $V_{SG}$ and W. Note that in the absence of drain-induced barrier lowering the OFF current, and hence the model, is independent of the transistor channel length (L). A main advantage of this empirical modeling framework is its applicability over different technology nodes. Table III provides the final forms of $A_0$ and GBW in strong and weak inversion regions.

Next, we used the expressions of the DC gain, GBW, and SR in Table III to determine the starting points of the design. We simplified our analysis by assuming an initial aspect ratio (i.e., W/L) of 100 and 50 for the p-type input and n-type output transistors, respectively. We made these assumptions because employing a large aspect ratio helps increase the voltage swing and decrease the flicker noise. With these assumptions, we then determined the combination of $\alpha$, $\beta$, and $I_D$ that satisfies the minimum opamp requirements for the DC gain, GBW, and SR in the strong and weak inversion regions, as shown in Fig. 9. Note that $\alpha$ and $\beta$ denote the current copying factors from the biasing branches into the input stage and the output stage, respectively. These factors are determined by the physical dimensions of the current copying transistors, and hence are the same in both strong and weak inversion regimes. The color map plots in Fig. 9 illustrate the calculated power consumption of the opamp. The grey markers in these plots show the values for $\alpha$, $\beta$, and $I_D$ that we used for prototyping the detection IC. We made a conservative decision in choosing these values to guarantee the robust operation of the prototype IC against process-voltage-temperature (PVT) variations. However, our calculations in Fig. 9 indicate the possibility of achieving a lower power consumption.

We implemented the detection IC using a standard 65 nm CMOS technology. In the final design, the opamp provides an open-loop gain of 102 (104) dB, GBW of 15 (3) MHz, and SR of 14.4 (2.2) V/$\mu$s in strong (weak) inversion region. The opamp operates on a dual supply of $\pm$1.65 V and has an input and output common-mode voltage of 0 V. The sampling ($C_s$) and integrating ($C_i$) capacitors of the modulator were 1.3 pF and 6.2 pF, implemented using MOM (metal-oxide-metal) capacitors. The capacitor values were chosen to significantly minimize the $k_B$T/C noise ($<-100$ dB noise floor). Fig. 10 shows the

TABLE III
EQUATIONS OF DC GAIN, GBW, AND SLEW RATE IN STRONG AND WEAK INVERSION

| Parameters | Weak inversion | Strong inversion |
|---|---|---|
| DC Gain (V/V) | $(\frac{2.3}{S^*})^2 \frac{1}{((\alpha+4)\lambda_n+\alpha\lambda_p)} \frac{\alpha}{(\lambda_n+\lambda_p)}$ | $[\sqrt{\frac{\mu_n C_{ox}(\frac{W}{L})_{20}}{2\beta I_D}} \sqrt{\frac{\mu_p C_{ox}(\frac{W}{L})_0}{\alpha I_D}}][\frac{4\alpha}{(\alpha+4)\lambda_n+\alpha\lambda_p}] \frac{1}{(\lambda_n+\lambda_p)}$ |
| GBW (Hz) | $(\frac{2.3}{S^*}) \frac{\alpha I_D}{2C_c}$ | $\frac{1}{C_c}\sqrt{\alpha I_D \mu_p C_{ox}(\frac{W}{L})_0}$ |
| Slew Rate (V/$\mu$s) | $min(\frac{\alpha I_D}{C_c}, \frac{\beta I_D}{(C_L+C_c)})$ | $min(\frac{\alpha I_D}{C_c}, \frac{\beta I_D}{(C_L+C_c)})$ |

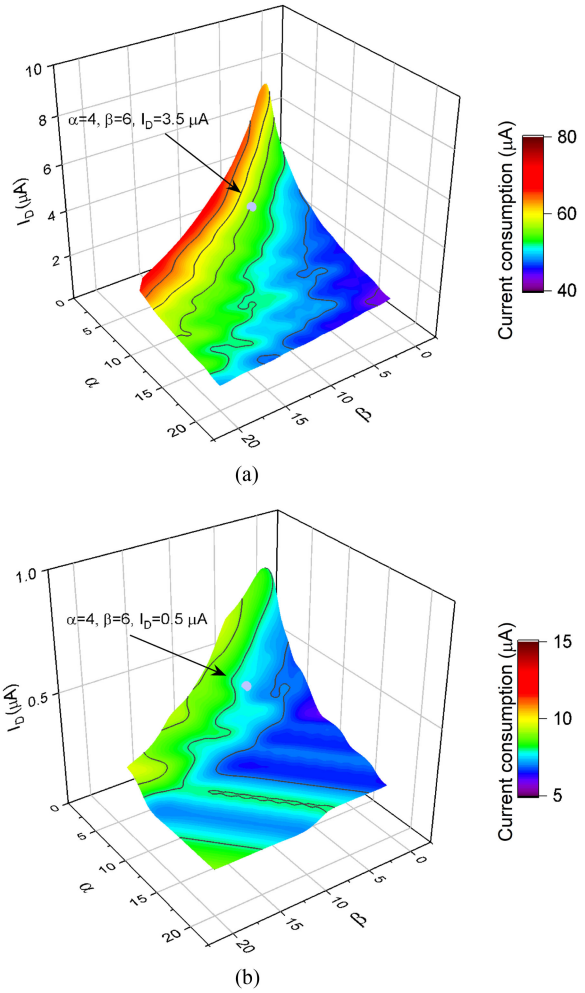


Fig. 9. Color map of the calculated power consumption in (a) strong and (b) weak inversion regions for a combination of $\alpha$, $\beta$, and $I_D$ that satisfies the minimum opamp requirements, shown in Fig. 6. The markers denote the parameters chosen for our prototype IC.

optical micrograph of the prototype detection IC, consisting of two readout channels.

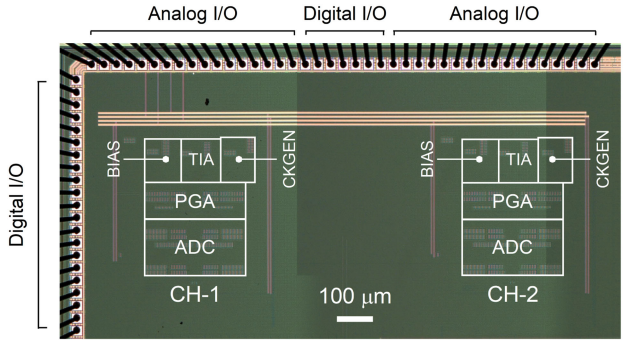


Fig. 10. Micrograph of the prototype biochip, consisting of two readout channels (CH-1 and CH-2).

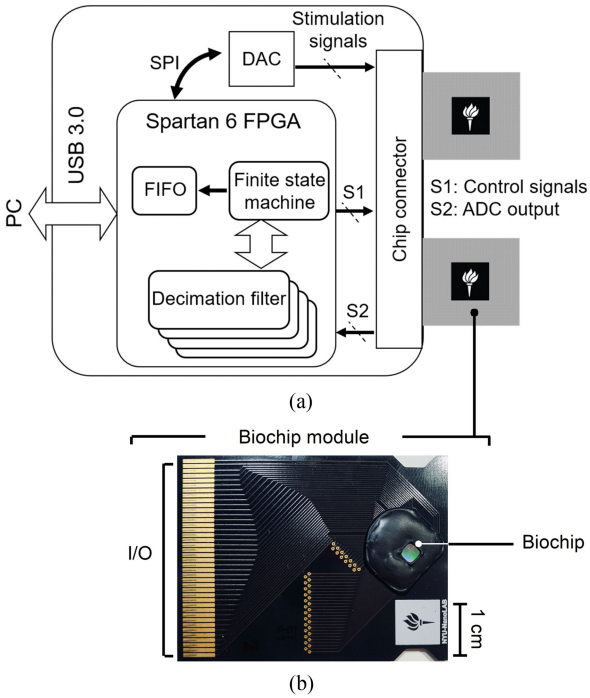


Fig. 11. (a) Block diagram of the electronics board used in the *in-vitro* measurements. (b) CMOS biochip module.

### *E. Electrical Measurements of ΔΣ Modulator*

Fig. 11 shows the schematic block diagram of the electronics board for interfacing with the biochip. The board consists of a Xilinx Spartan-6 FPGA (XEM6310-LX45), voltage level-shifters, and regulators. The FPGA performs three main functions. First, it provides all digital signals for the operation of the biochip. Second, it performs decimation and low-pass filtering (using a digital sinc$^3$ filter) on the 1-bit output data stream of the quantizer. Finally, it controls the communications, i.e., data transfer, between the board and an external computer. The measurement setup also consists of an external DAC (NI USB-6363X series), which generates the stimulation signals for the electrical verification of the ΔΣ modulator and the

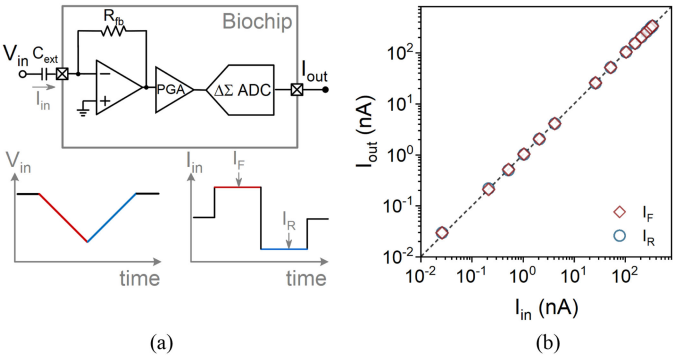


Fig. 12. (a) Measurement setup for verifying the linearity of the detection IC using DC current signals. (b) Measurements confirm the excellent linearity of the IC over a wider range of applied input DC currents, from 30 pA to 350 nA. The 1:1 dashed line is a guide for the eye.

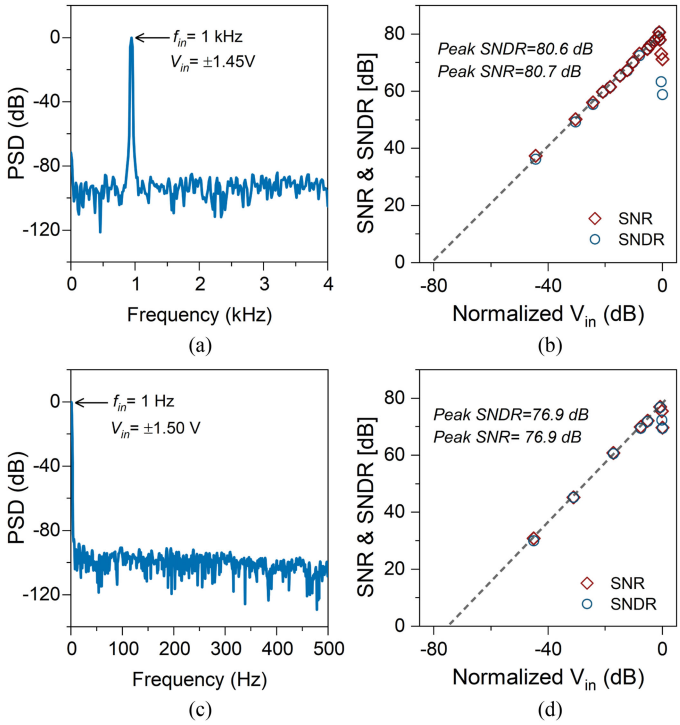


Fig. 13. Measured dynamic characteristics of the ADC in (a)–(b) strong inversion region and (c)–(d) weak inversion region. The dashed lines in (b) and (d) are guide for the eye.

*in-vitro* measurements of dopamine. While the prototype chip has two integrated readout channels, the electronics board has been developed to allow simultaneous operation of up to four readout channels. We used this capability for the multi-channel measurements of dopamine.

We studied the linearity of the modulator by applying a DC current signal with varying amplitudes to the detection IC. The DC current was generated by applying a voltage ramp to a high-precision capacitor, as shown in Fig. 12(a). The current amplitude was adjusted by varying the ramp rate of the input voltage or the size of the capacitor. The DC current was converted to a voltage signal by the on-chip R-TIA and was then digitized by the $\Delta\Sigma$ modulator. The measurement results in Fig. 12(b) indicate the excellent linearity of the detection IC over a wide range of applied DC currents (from 30 pA to 350 nA). The flexibility of the DT $\Delta\Sigma$ modulator in accommodating a wide range of oversampling clock frequencies is the key in enabling its high dynamic range.

Next, we measured the SNDR of the $\Delta\Sigma$ modulator under RPS and SPS modes (i.e., strong and weak inversion biasing conditions, respectively). Accounting for all non-idealities, including parasitics, our post-layout simulations indicated that the modulator could achieve an SNDR of about 80 dB using an OSR of 256. Hence, for both the SPS and RPS operating modes, we used this OSR, while adjusting the signal bandwidth and the oversampling frequencies accordingly. In particular, we set $f_b = 4$ kHz (500 Hz) and $f_s = 2.048$ MHz (250 kHz) for measuring the peak SNDR of the modulator under the RPS (SPS) mode. Fig. 13(a), (c) show the example of power spectral density (PSD) plots for two sine-wave voltage signals with a frequency of 1 kHz and 1 Hz, which were measured in RPS and SPS modes, respectively. We repeated these measurements for multiple sine-waves with varying amplitudes. From their corresponding PSD plots, we then calculated the SNR and SNDR of the $\Delta\Sigma$ modulator in RPS and SPS modes, corresponding to an ENOB close to 13 bits. Fig. 13(b), (d) show the summary of the SNR and SNDR measurements. We note that the measured SNR and SNDR in Fig. 13(d) represent the lower bound of the modulator performance in SPS mode as the measurements were limited by the higher noise of the voltage signals generated by the DAC at low frequencies.

### *F. Noise Analysis*

Before the *in-vitro* measurements, it is insightful to discuss the noise performance of our sensing unit, as it has bearing on the minimum detectable dopamine concentration in SPS and RPS measurements. Fig. 14(a) shows the simplified noise model of our sensing unit. The input-referred noise current of the biochip ($\overline{I_{n,total}}$) can be expressed as

$$\overline{I_{n,total}^2} = \overline{I_{th,s}^2} + \overline{I_{sh,s}^2} + \overline{I_{n,TIA}^2} + \frac{\overline{V_{n,PGA}^2}}{R_{fb}^2} + \frac{\overline{V_{n,\Delta\Sigma}^2}}{A_{PGA}^2 \times R_{fb}^2} \quad (5)$$

The first line in equation 5 represents the noise contribution of the NG micro-sensor due to the thermal noise ($\overline{I_{th,s}^2}$) and the shot noise ($\overline{I_{sh,s}^2}$) [11]. Using the data in Table II for a 625 $\mu$m$^2$ NG sensor and assuming a solution resistance ($R_{sol}$) of $\approx$ 200 k$\Omega$, the estimated $\overline{I_{th,s}}$ and $\overline{I_{sh,s}}$ are about 16 (125) and 9 (53) pA$_{rms}$ (fA$_{rms}$) in RPS (SPS) measurements.

The second line in equation 5 represents the noise contributions of the R-TIA, PGA, and ADC. The feedback resistor and the opamp determine the noise of the R-TIA [47]. Figs. 14(b)–(c) show the simplified noise models of the opamp (i.e., $\overline{V_{n,OP}^2}$), and PGA (i.e., $\overline{V_{n,PGA}^2}$). Table IV gives the calculated noise contributions of the R-TIA and PGA.

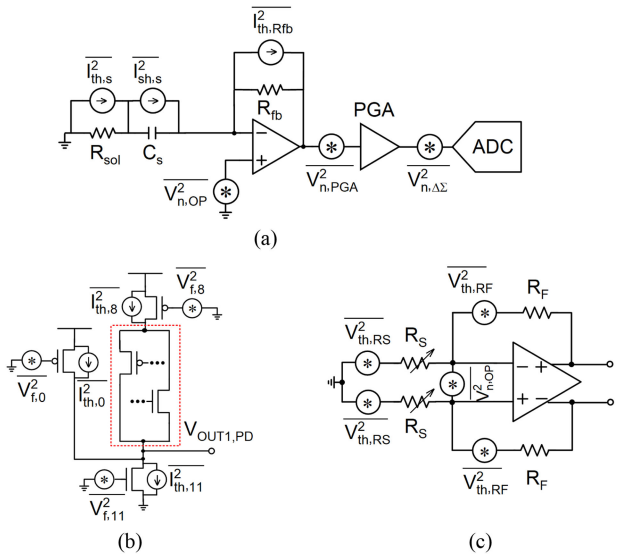


Fig. 14. (a) Illustration of major noise sources of the sensing unit. Simplified noise models of the (b) opamp, and (c) PGA.

TABLE IV
NOISE ANALYSIS OF THE SENSING UNIT

| | SPS | RPS |
|---|---|---|
| Bandwidth | 0-100 Hz | 0-5 kHz |
| ADC | 38 $fA_{rms}$ | 23 $pA_{rms}$ |
| R-TIA | >100 & <600 $fA_{rms}$* | 9 $pA_{rms}$ |
| PGA | 10 $fA_{rms}$ | 8 $pA_{rms}$ |
| $\overline{I_{th,s}}$ | 125 $fA_{rms}$ | 16 $pA_{rms}$ |
| Total measured noise | 345 $fA_{rms}$ | 67 $pA_{rms}$ |

*Estimated noise based on the data sheet of the SR570 amplifier.

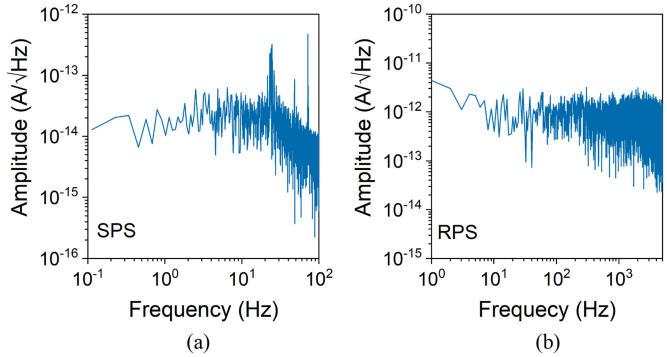


Fig. 15. Measured noise performance of the sensing unit under the (a) SPS and (b) RPS modes. The integrated noise for the frequency range shown in (a) and (b) are about 345 $fA_{rms}$ and 67 $pA_{rms}$, respectively.

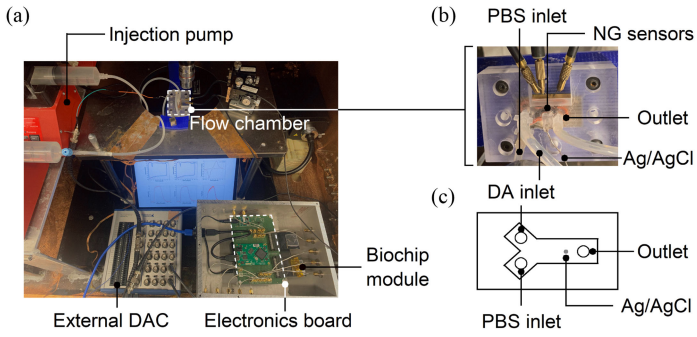


Fig. 16. Photographs of (a) the *in-vitro* measurement setup, and (b) the custom-made microfluidic chamber. (c) Top-view schematic of the Y-shaped microfluidic chamber.

For a modulator with negligible quantization error, its noise will be dominated by the noise of the opamp in the modulator (e.g., see Ref. [8]). In our design, however, the quantization error dominates the noise contribution of the modulator to $\overline{I_{n,total}}$. From the measured peak SNDR data in Fig. 13, the quantization error of the $\Delta\Sigma$ modulator is about 96 (150) $\mu V_{rms}$ in RPS (SPS).

Next, we measured the input-referred noise current of the sensing unit under the SPS and RPS modes, shown in Figs. 15(a)–(b). In these measurements, an NG micro-sensor with a geometric area of 580 $\mu m^2$ was connected to the detection IC. The measurements were made at 0 V dc bias. As a result, the potentials of the sensor, and the reference electrode (RE) were 0 V. The data give a total noise of about 67 $pA_{rms}$ and 345 $fA_{rms}$ for RPS and SPS. The measured noise performance agree with those expected from the calculations (see Table IV). We note that the spectral noise behavior of the SR570 amplifier dominated the measured noise in SPS, shown in Fig. 15(a).

Our noise analysis and measurement in the RPS mode indicate that the collective contribution of the NG micro-sensor, R-TIA, and PGA becomes comparable to that of the ADC. This translates into at least a factor of two loss in the limit of detection as expected per the calculations in Table II. Moreover, in the SPS mode, the external R-TIA circuit, and the NG micro-sensor are the major factors in limiting the noise performance of the sensing unit. However, the measured noise performance still satisfies the requirement for detecting 100 nM dopamine in SPS experiments, as listed in Table II.

## IV. IN-VITRO MEASUREMENTS OF DOPAMINE

### A. Measurement Setup and Methods

We verified the utility of our detection IC for measuring low concentrations of bio-analytes through *in-vitro* measurements of dopamine. Fig. 16(a) shows the schematic of the *in-vitro* measurement setup, consisting of a flow chamber, injection pumps, the interface electronics board, and an external computer. A custom-made microfluidic chamber, as shown in Figs. 16(b)–(c), was used for delivering bio-analytes. The microfluidic chamber has a Y-shaped configuration with two inlets and one outlet. It also holds the Ag/AgCl reference electrode.

Given the small current of the micro-sensors, a two-electrode measurement scheme is suitable for voltammetry measurements [1]. In our SPS and RPS experiments, the potential waveform is applied to the sensor, as shown in Fig. 17. Micromanipulator probes, as shown in Fig. 16(b), were used for connecting the NG micro-sensors to the detection IC. A custom-made

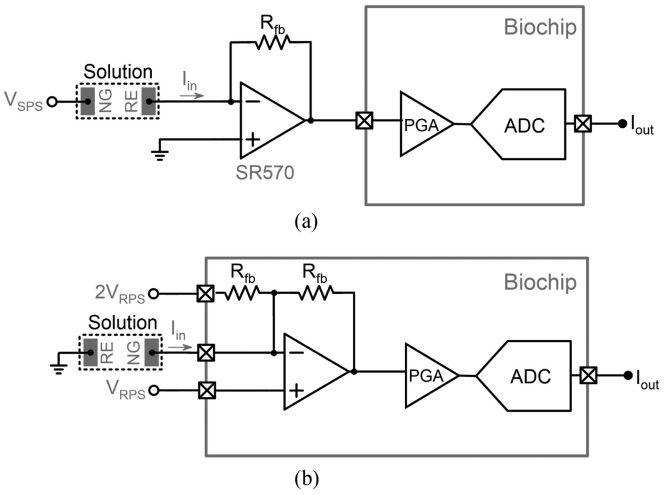


Fig. 17. Schematic illustrations of the sensing unit configuration for the (a) SPS, and (b) RPS measurements of dopamine.

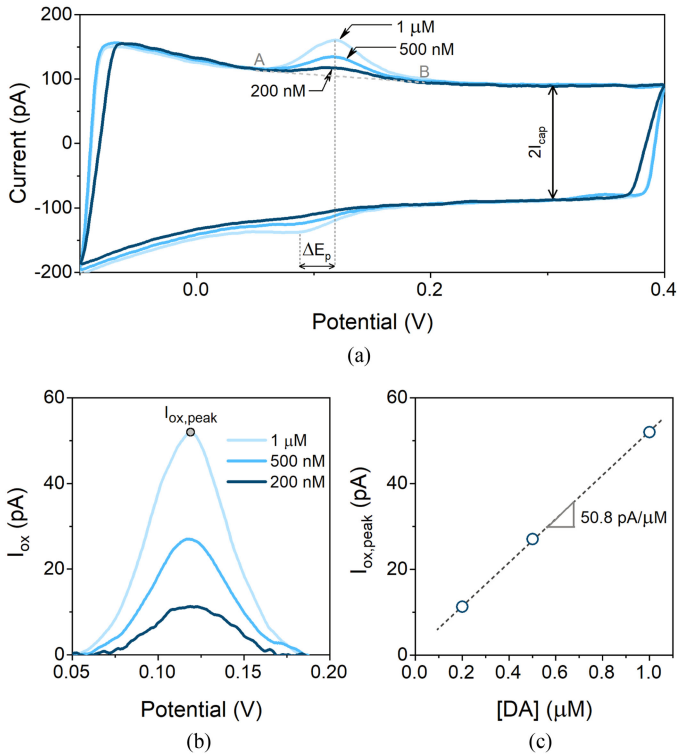


Fig. 18. (a) *In-vitro* measurements of dopamine under SPS conditions with a ramp rate of 0.1 V/s. (b) The background-subtracted oxidation current for three dopamine concentrations obtained from the measured data in panel (a). (c) The calibration curve confirms the linearity of the sensor under SPS. A linear fit to the data gives a sensitivity of 50.8 pA/$\mu$M.

user interface program was developed in MATLAB for data acquisition and data analysis.

For the *in-vitro* experiments, we used NG micro-sensors with a geometric area of 360 and 580 $\mu m^2$. Phosphate buffered solution (PBS) was used as the buffer solution. PBS (1X concentration, pH of 7.4) was prepared by dissolving 8 g of sodium chloride, 1.44 g of sodium phosphate dibasic, 240 mg of potassium phosphate monobasic, and 200 mg potassium chloride in 1 L de-ionized water. A concentrated (2 mM) dopamine solution was prepared by dissolving dopamine hydrochloride powder in 1X PBS. Dopamine solutions with smaller concentrations were then prepared by diluting the 2 mM stock in 1X PBS. All chemicals were purchased from Sigma Aldrich.

### *B. Dopamine SPS Measurements*

We performed dopamine sensing under SPS conditions using a 580 $\mu m^2$ NG micro-sensor. Before each SPS experiment, the microfluidic chamber was filled with a dopamine solution of known concentration. This experimental design mimics the baseline dopamine (i.e., tonic mode) in the brain. We then applied a triangular potential waveform (see Fig. 1(a)) and recorded the sensor response. The waveform had the LPL and UPL of $-0.1$ V and 0.4 V, and was ramped at $\nu = 0.1$ V/s and repeated every 10 s (i.e., $t_d = 0$ s). Fig. 18(a) shows the SPS measurement results for three dopamine concentrations. The redox current peaks of dopamine are visible and well within the potential range that we used for the SPS measurements.

During the forward scan, dopamine is oxidized to dopamine-ortho-quinone (DoQ), giving two electrons to the sensor. During the reverse scan, DoQ is reduced back to dopamine, taking two electrons from the sensor. These electron transfer events result in a redox current, where its amplitude is a measure of the bio-analyte concentration in the solution. However, since the tonic dopamine is always present in the brain, it is not possible to independently measure the background current (i.e., the sensor response without dopamine) during the sensing measurements. Hence, this characteristics of tonic dopamine prevents resolving the redox peaks through the background subtraction scheme, as shown in Figs. 1(b)–(d). Therefore, to obtain the absolute amplitude of the redox current, one approach is to estimate the background signal and then subtract it from the total current. Based on the shape of the background current of our NG micro-sensors, we used simple linear regression for removing its contribution to the total current (see the grey dashed line between points "A" and "B" in Fig. 18(a)). The visible redox peaks of dopamine even at low concentrations allowed the implementation of this analysis method. In Fig. 18(b), we show the background-subtracted oxidation current peaks ($I_{ox}$) measured for three different known dopamine concentrations. These measurements confirm the ability of the NG micro-sensor and the detection IC for measuring dopamine with concentrations as low as 200 nM under the SPS conditions. The plot of $I_{ox,peak}$ against the dopamine concentration shows the linearity of the NG micro-sensor. Further, the small y-intercept of this linear fit (i.e., $1.3 \pm 0.4$ pA) indicates that the simple linear regression in Fig. 18(a) provided a good estimate for the subtraction of the background current in these SPS experiments.

The separation of the redox peak potentials ($\Delta E_p$) gives important information about the nature of the redox reactions. A $\Delta E_p$ close to $58/n$ mV (at 25 °C) suggests a Nernstian (reversible) reaction as a result of rapid electron transfer at the sensor surface [1]; $n$ is the number of electrons involved in the

redox reaction ($n = 2$ for the dopamine redox reaction). The data in Fig. 18(a) show $\Delta E_p = 30 \pm 1$ mV, indicating fast electron transfer properties of our NG micro-sensors.

### C. Dopamine RPS Measurements

We also studied the performance of the sensing unit for detecting dopamine under RPS measurement conditions. These *in-vitro* experiments were aimed at simulating the transient (phasic) dopamine release. Specifically, the phasic dopamine levels represent the changes in the dopamine concentration relative to the background. Therefore, in our RPS experiments, PBS was first injected into the chamber (at 2 ml/min), while recording the sensor response (i.e., the background current). Taking advantage of the Y-shaped configuration of the microfluidic chamber, the flow was then switched to deliver dopamine solutions with a known concentration (at 6 ml/min) without interrupting the recording of the sensor current. The RPS measurements were performed using an N-shaped potential waveform with $\nu = 200$ V/s and a temporal resolution of 100 ms, as shown in the inset in Fig. 19(d).

Fig. 19(a) shows the measured background current (before injecting dopamine; marked as 0 $\mu$M) and the total current (after injecting 1 $\mu$M dopamine) using the N-shaped waveform. While the SPS and RPS measurements in Figs. 18–19 were made using the same NG micro-sensor, the sensor capacitance (calculated from $I_{cap}/\nu$) in RPS is about 25% smaller than in SPS. We attribute this observation to the frequency-dependence of the sensor capacitance.

The cyclic voltammograms of the phasic dopamine were then obtained by subtracting the background current from the total current. Fig. 19(b) shows the cyclic voltammograms of dopamine at different concentrations as low as 50 nM. For better illustration, we plotted the cyclic voltammogram of the 50 nM dopamine in Fig. 19(c), showing the well-defined oxidation and reduction peaks. These experiments confirm the ability of our sensing unit for measuring low concentrations of dopamine under RPS conditions. Plotting $I_{ox,peak}$ against the dopamine concentration, as shown in Fig. 19(d), confirms the linearity of the NG micro-sensor response.

In our RPS experiments, the use of an N-shaped waveform, in lieu of a triangular one, greatly benefited the detection of low-concentration dopamine. Using a triangular waveform in RPS measurements with our NG micro-sensors, we consistently observed the slight change of $I_{quinone}$ (typically $<1$ nA) upon switching from the PBS to the dopamine solution. At low concentrations, where the redox current of dopamine is small, this slight change of $I_{quinone}$ could be detrimental for resolving the dopamine voltammogram reliably. We attribute the observed change of $I_{quinone}$ to a slight change in the local steady-state pH of the solution on the sensor surface upon injecting dopamine. The basis for this speculation is that the dopamine redox reaction involves protons ($H^+$). Further, the quinone-like species are highly sensitive to the change of pH, resulting in a noticeable variation of $I_{quinone}$ due to pH change [48]. The N-shaped waveform used in our RPS experiments mitigated the interference of $I_{quinone}$ with the oxidation current peak of dopamine. Hence, we were able to resolve the redox peaks of dopamine reliably at low concentrations without invoking complicated data analysis techniques.

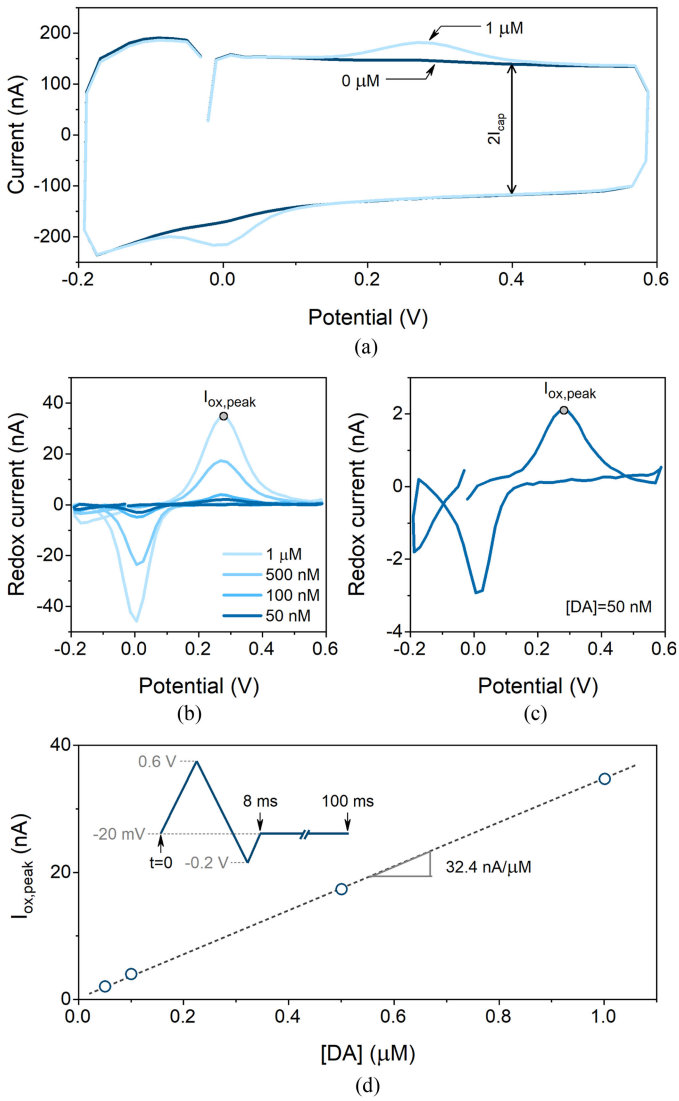


Fig. 19. (a) Current of the NG micro-sensor measured *in-vitro* under RPS conditions with and without dopamine. (b) Measured background-subtracted current (i.e., redox current) for four dopamine concentrations obtained from the RPS data. (c) Cyclic voltammogram of 50 nM dopamine in RPS. (d) Calibration curve indicates the linearity of the micro-sensor in RPS. A linear fit to the data gives a sensitivity of 32.4 nA/$\mu$M. The inset shows the illustration of the N-shaped voltage waveform used in RPS measurements.

Lastly, we demonstrated the capability of our sensing system for supporting multi-channel measurements of dopamine. Due to the limitation of the SR570 amplifier, which provides only one readout channel, we performed the multi-channel measurements of dopamine under the RPS conditions. Fig. 20(a) shows the typical background current curves of three NG micro-sensors, fabricated on the same substrate. These sensors had a geometric area of 360 $\mu m^2$. Figs. 20(b)–(c) show the typical cyclic voltammograms obtained using these sensors for dopamine with a concentration of 1 $\mu$M and 50 nM, respectively. The similar

TABLE V
PERFORMANCE SUMMARY AND COMPARISON WITH THE STATE-OF-THE-ART

| | This work | JSSC'09 [11] | JSSC'14 [12] | TBioCAS'16 [14] | TBioCAS'12 [5] |
|---|---|---|---|---|---|
| Process Technology | 65 nm | 0.5 $\mu$m | 0.35 $\mu$m | 65 nm | 0.35 $\mu$m |
| Sensor type | NG micro-sensor | Carbon fiber | Carbon fiber | Carbon fiber | Gold |
| Power Supply | $\pm$1.65 V | $\pm$1.25 V | 2.5 V | 1.2, 3.0 V | 3.3 V |
| ADC architecture | $2^{nd}$- DT $\Delta\Sigma$ Fully differential | $3^{rd}$- CT $\Delta\Sigma$ Single-ended | $3^{rd}$- CT $\Delta\Sigma$ Single-ended | SAR Single-ended | Single slope Single-ended |
| Channel size | 350 $\times$ 300 $\mu m^2$ | 920 $\times$ 180 $\mu m^2$ | 984 $\times$ 113 $\mu m^2$ | N/A | 200 $\times$ 200 $\mu m^2$ |
| Input current range | $\pm$ 350 nA | $\pm$ 750 nA | $\pm$ 950 nA | $\pm$ 430 nA | $\pm$ 350 nA |
| Recording bandwidth | Adjustable: up to 5 kHz | Adjustable: up to 5 kHz | Adjustable: up to 5 kHz | 2 kHz | Adjustable: up to 500 Hz |
| ADC clock frequency ($f_s$) | Adjustable: 64 kHz-2.5 MHz | 730 kHz | 625 kHz | 4 kHz | Adjustable: 100 Hz-1 kHz |
| Measured peak SNDR | 80.6 dB | - | 70.7 dB | 50.3 dB | 52 dB |
| ADC current consumption | 166 $\mu$A in RPS mode* 28.54 $\mu$A in SPS mode† | 30.4 $\mu$A | 3.72 $\mu$A | 4.8 $\mu$A | 57 $\mu$A |
| Number of channels | 2 | 4 | 1 | 1 | 96 |
| Lowest [DA] measured *in-vitro* at a temporal resolution | 50 nM at 100 ms 200 nM at 10 s | 250 nM at 200 ms | 125 nM at 100-200 ms | 250 nM at 100 ms | 20 $\mu$M at amperometry |
| Testing method | *In-vitro* | *In-vitro* and *in-vivo* | *In-vitro* and *in-vivo* | *In-vitro* | *In-vitro* |

*52.5 $\mu$A for R-TIA and 80.4 $\mu$A for PGA.
†14.5 $\mu$A for PGA.

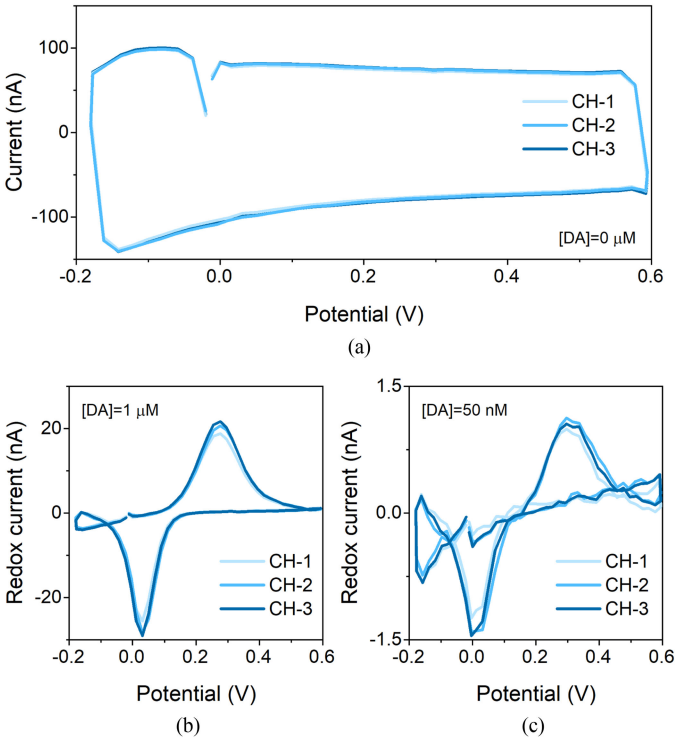


Fig. 20. (a) Background currents of three NG micro-sensors measured simultaneously in RPS. The corresponding voltammograms of the micro-sensors from the RPS measurements of (b) 1 $\mu$M and (c) 50 nM dopamine.

characteristics of these sensors indicate the advantage of microfabrication for producing an array of miniaturized sensors, where the consistency of the sensor characteristics within the array is critical for the development of a sensing system. Further, we note that the sensors used in the multi-channel measurements were produced at a different fabrication run than the sensor in Figs. 18–19; but the processing conditions between the two sensor fabrication runs were similar. Despite having been produced at different runs, our NG micro-sensors show reproducible characteristics in terms of both the background current and the redox current. This feature is highly beneficial for the future optimization of the detection IC around the characteristics of the NG micro-sensors.

## V. CONCLUSION

Advances in the development of planar micro-sensors from NG carbon open an opportunity for enhancing the capabilities of electrochemical biochips. The reported results in this paper show a simple strategy for implementing a configurable CMOS biochip by leveraging the advantageous features of NG micro-sensors. In particular, the biochip can be configured on-demand for an optimal power consumption depending on the temporal resolution requirements of the sensing experiments while maintaining the required performance. This feature distinguishes our biochip from the previously reported detection ICs used for measuring dopamine (see Table V). We anticipate that the high precision of our detection IC could also benefit sensing experiments that employ electrochemical sensors made of other materials besides NG carbon (e.g., carbon fiber, gold).

While our study showed the possibility of making an electrochemical sensing unit with enhanced functionality, future studies must focus on developing strategies for scaling up this sensing unit into a large-scale lab-on-a-chip system while further improving the performance. An obvious next step is the optimization of the detection IC by implementing compact and low-noise front-end amplification circuits for interfacing with the NG micro-sensors in SPS measurements. The low-noise current amplifier circuit in Ref. [49] is a promising candidate for this application. Further, our calculations in Fig. 9 show a path for lowering the power consumption of the $\Delta\Sigma$ modulator in future implementations. Another important direction is the development of strategies for integrating many NG micro-sensors on top of the CMOS biochip. Two possible approaches can be pursued to achieve this objective. The first approach is to grow NG carbon materials directly on the CMOS biochip surface, which must be done at sufficiently low temperatures compatible with post-CMOS fabrication ($\leq$400 °C). The second approach involves the deterministic assembly of micron-scale NG carbon islands by transferring them from a host substrate to precise locations on the surface of the CMOS biochip. Lastly, future studies

must also develop a detailed understanding of the microscopic mechanisms of noise in NG micro-sensors. This knowledge is essential for a systematic engineering of their material and device structure to achieve a desired noise performance.

## ACKNOWLEDGMENT

The authors acknowledge United Microelectronics Corporation (UMC) for the support and fabrication of the CMOS chip. The sensor fabrication was performed at the City University of New York Advanced Science Research Center (ASRC) Nanofabrication Facility.

## REFERENCES

[1] A. J. Bard, L. R. Faulkner, J. Leddy, and C. G. Zoski, *Electrochemical Methods: Fundamentals and Applications*, vol. 2, Hoboken, NJ, USA: Wiley, 1980.

[2] P. M. Levine, P. Gong, R. Levicky, and K. L. Shepard, "Active CMOS sensor array for electrochemical biomolecular detection," *IEEE J. Solid-State Circuits*, vol. 43, no. 8, pp. 1859–1871, Aug. 2008.

[3] M. H. Nazari, H. Mazhab-Jafari, L. Leng, A. Guenther, and R. Genov, "192-channel cmos neurochemical microarray," in *Proc. IEEE Custom Integr. Circuits Conf.*, 2010, pp. 1–4.

[4] A. Manickam, A. Chevalier, M. McDermott, A. D. Ellington, and A. Hassibi, "A CMOS electrochemical impedance spectroscopy (EIS) biosensor array," *IEEE Trans. Biomed. Circuits Syst.*, vol. 4, no. 6, pp. 379–390, Dec. 2010.

[5] M. H. Nazari, H. Mazhab-Jafari, L. Leng, A. Guenther, and R. Genov, "CMOS neurotransmitter microarray: 96-channel integrated potentiostat with on-die microsensors," *IEEE Trans. Biomed. Circuits Syst.*, vol. 7, no. 3, pp. 338–348, Jun. 2012.

[6] R. Genov, M. Stanacevic, M. Naware, G. Cauwenberghs, and N. Thakor, "16-channel integrated potentiostat for distributed neurochemical sensing," *IEEE Trans. Circuits Syst. I: Reg. Papers*, vol. 53, no. 11, pp. 2371–2376, Nov. 2006.

[7] D. L. Bellin, H. Sakhtah, Y. Zhang, A. Price-Whelan, L. E. Dietrich, and K. L. Shepard, "Electrochemical camera chip for simultaneous imaging of multiple metabolites in biofilms," *Nature Commun.*, vol. 7, no. 1, pp. 1–10, 2016.

[8] A. Manickam *et al.*, "A CMOS Electrochemical Biochip With 32 × 32 Three-Electrode Voltammetry Pixels," *IEEE J. Solid-State Circuits*, vol. 54, no. 11, pp. 2980–2990, Nov. 2019.

[9] A. Manickam *et al.*, "11.2 A CMOS biosensor array with 1024 3-electrode voltammetry pixels and 93 dB dynamic range," in *Proc. IEEE Int. Solid-State Circuits Conf.*, 2019, pp. 192–194.

[10] M. Roham *et al.*, "A wireless IC for wide-range neurochemical monitoring using amperometry and fast-scan cyclic voltammetry," *IEEE Trans. Biomed. Circuits Syst.*, vol. 2, no. 1, pp. 3–9, Mar. 2008.

[11] M. Roham *et al.*, "A wireless IC for time-share chemical and electrical neural recording," *IEEE J. Solid-State Circuits*, vol. 44, no. 12, pp. 3645–3658, Dec. 2009.

[12] B. Bozorgzadeh, D. P. Covey, C. D. Howard, P. A. Garris, and P. Mohseni, "A neurochemical pattern generator SoC with switched-electrode management for single-chip electrical stimulation and 9.3 $\mu$W, 78 pA rms, 400 V/s fscv sensing," *IEEE J. Solid-State Circuits*, vol. 49, no. 4, pp. 881–895, Apr. 2014.

[13] B. Nasri *et al.*, "Hybrid cmos-graphene sensor array for subsecond dopamine detection," *IEEE Trans. Biomed. Circuits Syst.*, vol. 11, no. 6, pp. 1192–1203, Dec. 2017.

[14] C. I. Dorta-Quiñones, X. Y. Wang, R. K. Dokania, A. Gailey, M. Lindau, and A. B. Apsel, "A wireless FSCV monitoring IC with analog background subtraction and UWB telemetry," *IEEE Trans. Biomed. Circuits Syst.*, vol. 10, no. 2, pp. 289–299, Apr. 2015.

[15] J. E. Koehne *et al.*, "Carbon nanofiber electrode array for electrochemical detection of dopamine using fast scan cyclic voltammetry," *Analyst*, vol. 136, no. 9, pp. 1802–1805, 2011.

[16] M. Bariya, H. Y. Y. Nyein, and A. Javey, "Wearable sweat sensors," *Nature Electron.*, vol. 1, no. 3, pp. 160–171, 2018.

[17] T. Wu, A. Alharbi, R. Kiani, and D. Shahrjerdi, "Quantitative principles for precise engineering of sensitivity in graphene electrochemical sensors," *Adv. Mater.*, vol. 31, no. 6, 2019, Art. no. 1805752.

[18] S. Demuru *et al.*, "Scalable nanostructured carbon electrode arrays for enhanced dopamine detection," *ACS Sensors*, vol. 3, no. 4, pp. 799–805, 2018.

[19] R. L. McCreery, "Advanced carbon electrode materials for molecular electrochemistry," *Chem. Rev.*, vol. 108, no. 7, pp. 2646–2687, 2008.

[20] E. Cuniberto *et al.*, "Nano-engineering the material structure of preferentially oriented nano-graphitic carbon for making high-performance electrochemical micro-sensors," *Scientific Rep.*, vol. 11, no. 9444, pp. 1–11, 2020.

[21] A. A. Grace, "The tonic/phasic model of dopamine system regulation: its relevance for understanding how stimulant abuse can alter basal ganglia function," *Drug Alcohol Dependence*, vol. 37, no. 2, pp. 111–129, 1995.

[22] C. A. Owesson-White *et al.*, "Sources contributing to the average extracellular concentration of dopamine in the nucleus accumbens," *J. Neurochemistry*, vol. 121, no. 2, pp. 252–262, 2012.

[23] Z. B. Rosen, S. Cheung, and S. A. Siegelbaum, "Midbrain dopamine neurons bidirectionally regulate CA3-CA1 synaptic drive," *Nature Neurosci.*, vol. 18, no. 12, 2015.

[24] R. J. Wickham *et al.*, "Advances in studying phasic dopamine signaling in brain reward mechanisms," *Front. Biosci. (Elite edition)*, vol. 5, pp. 982–999, 2013.

[25] A. S. Hart, R. B. Rutledge, P. W. Glimcher, and P. E. Phillips, "Phasic dopamine release in the rat nucleus accumbens symmetrically encodes a reward prediction error term," *J. Neurosci.*, vol. 34, no. 3, pp. 698–704, 2014.

[26] Y. Oh *et al.*, "Tracking tonic dopamine levels in vivo using multiple cyclic square wave voltammetry," *Biosensors Bioelectron.*, vol. 121, pp. 174–182, 2018.

[27] C. W. Atcherley, K. M. Wood, K. L. Parent, P. Hashemi, and M. L. Heien, "The coaction of tonic and phasic dopamine dynamics," *Chem. Commun.*, vol. 51, no. 12, pp. 2235–2238, 2015.

[28] J. Delforge, M. Bottlaender, S. Pappata, C. Loch, and A. Syrota, "Absolute quantification by positron emission tomography of the endogenous ligand," *J. Cerebral Blood Flow Metabolism*, vol. 21, no. 5, pp. 613–630, 2001.

[29] A. C. Schmidt, X. Wang, Y. Zhu, and L. A. Sombers, "Carbon nanotube yarn electrodes for enhanced detection of neurotransmitter dynamics in live brain tissue," *Acs Nano*, vol. 7, no. 9, pp. 7864–7873, 2013.

[30] J. A. Johnson, N. T. Rodeberg, and R. M. Wightman, "Measurement of basal neurotransmitter levels using convolution-based nonfaradaic current removal," *Analytical Chemistry*, vol. 90, no. 12, pp. 7181–7189, 2018.

[31] A. Hermans, R. B. Keithley, J. M. Kita, L. A. Sombers, and R. M. Wightman, "Dopamine detection with fast-scan cyclic voltammetry used with analog background subtraction," *Analytical Chemistry*, vol. 80, no. 11, pp. 4040–4048, 2008.

[32] S. D O'Connor, G. T. Olsen, and S. E. Creager, "A Nernstian electron source model for the ac voltammetric response of a reversible surface redox reaction using large-amplitude ac voltages," *J. Electroanalytical Chemistry*, vol. 466, no. 2, pp. 197–202, 1999.

[33] Y. Zhu *et al.*, "Carbon-based supercapacitors produced by activation of graphene," *Science*, vol. 332, no. 6037, pp. 1537–1541, 2011.

[34] N. T. Rodeberg, S. G. Sandberg, J. A. Johnson, P. E. Phillips, and R. M. Wightman, "Hitchhiker's guide to voltammetry: acute and chronic electrodes for in vivo fast-scan cyclic voltammetry," *ACS Chem. Neurosci.*, vol. 8, no. 2, pp. 221–234, 2017.

[35] R. B. Keithley and R. M. Wightman, "Assessing principal component regression prediction of neurochemicals detected with fast-scan cyclic voltammetry," *ACS Chem. Neuroscience*, vol. 2, no. 9, pp. 514–525, 2011.

[36] J. A. Johnson, N. T. Rodeberg, and R. M. Wightman, "Failure of standard training sets in the analysis of fast-scan cyclic voltammetry data," *ACS Chem. Neurosci.*, vol. 7, no. 3, pp. 349–359, 2016.

[37] K. T. Kishida *et al.*, "Subsecond dopamine fluctuations in human striatum encode superposed error signals about actual and counterfactual reward," *Proc. Nat. Acad. Sci.*, vol. 113, no. 1, pp. 200–205, 2016.

[38] B. Bozorgzadeh, D. R. Schuweiler, M. J. Bobak, P. A. Garris, and P. Mohseni, "Neurochemostat: A neural interface SoC with integrated chemometrics for closed-loop regulation of brain dopamine," *IEEE Trans. Biomed. Circuits Syst.*, vol. 10, no. 3, pp. 654–667, Jun. 2015.

[39] H. Ji *et al.*, "Capacitance of carbon-based electrical double-layer capacitors," *Nature Commun.*, vol. 5, pp. 1–7, 2014.

[40] P. Takmakov, C. J. McKinney, R. M. Carelli, and R. M. Wightman, "Instrumentation for fast-scan cyclic voltammetry combined with electrophysiology for behavioral experiments in freely moving animals," *Rev. Scientific Instruments*, vol. 82, no. 7, 2011, Art. no. 074302.

[41] A. Yukawa, "A cmos 8-bit high-speed a/d converter ic," *IEEE J. Solid-State Circuits*, vol. 20, no. 3, pp. 775–779, Jun. 1985.

[42] R. Schreier *et al.*, *Understanding Delta-Sigma Data Converters*, vol. 74, Piscataway, NJ, USA: IEEE press, 2005.
[43] P. Malcovati, S. Brigati, F. Francesconi, F. Maloberti, P. Cusinato, and A. Baschirotto, "Behavioral modeling of switched-capacitor sigma-delta modulators," *IEEE Trans. Circuits Syst. I: Fundam. Theory Appl.*, vol. 50, no. 3, pp. 352–364, Mar. 2003.
[44] B. P. Brandt, D. E. Wingard, and B. A. Wooley, "Second-order sigma-delta modulation for digital-audio signal acquisition," *IEEE J. Solid-State Circuits*, vol. 26, no. 4, pp. 618–627, Apr. 1991.
[45] R. Hogervorst, J. P. Tero, R. G. Eschauzier, and J. H. Huijsing, "A compact power-efficient 3 V CMOS rail-to-rail input/output operational amplifier for VLSI cell libraries," *IEEE J. Solid-State Circuits*, vol. 29, no. 12, pp. 1505–1513, Dec. 1994.
[46] A. Khakifirooz, "Transport enhancement techniques for nanoscale MOSFETs," Ph.D. dissertation, Massachusetts Institute of Technology, Cambridge, MA, USA, 2008.
[47] M. Crescentini, M. Bennati, M. Carminati, and M. Tartagni, "Noise limits of CMOS current interfaces for biosensors: A review," *IEEE Trans. Biomed. Circuits Syst.*, vol. 8, no. 2, pp. 278–292, Apr. 2013.
[48] P. Takmakov, M. K. Zachek, R. B. Keithley, E. S. Bucher, G. S. McCarty, and R. M. Wightman, "Characterization of local pH changes in brain using fast-scan cyclic voltammetry with carbon microelectrodes," *Analytical Chemistry*, vol. 82, no. 23, pp. 9892–9900, 2010.
[49] G. Ferrari, M. Farina, F. Guagliardo, M. Carminati, and M. Sampietro, "Ultra-low-noise CMOS current preamplifier from DC to 1 MHz," *Electron. Lett.*, vol. 45, no. 25, pp. 1278–1280, 2009.

**Kae-Dyi You** (Student Member, IEEE) received the B.S. degree from National Cheng Kung University, Tainan, Taiwan, in 2006 and the M.S. degree from National Chiao Tung University, Hsinchu, Taiwan, in 2009, both in electrical engineering. He is currently pursuing the Ph.D. degree in electrical and computer engineering at New York University (NYU), New York, NY, USA. From 2009 to 2016, he held a position as an Analog and Mixed-Signal IC Design Engineer in Taiwan, where he was involved in full chip design and mass production of three main projects: fingerprint sensing front-end circuits, advanced audio codec systems, and the design of high-speed serial link ICs. His current research interests include design and implementation of power- and area-efficient CMOS read-out circuits for brain interfaces and heterogeneous biosensing microsystems.

**Edoardo Cuniberto** received the B.S. degree in physics engineering from Politecnico di Torino, Turin, Italy, and an international M.S. degree in nanotechnologies for ICTs from Politecnico di Torino, Turin, Italy, Institut Polytechnique de Grenoble, Grenoble, France and École Polytechnique Fédérale de Lausanne (EPFL), Lausanne, Switzerland, in 2015 and 2017, respectively. He is currently working toward the Ph.D. degree in electrical and computer engineering at New York University (NYU), New York, NY, USA. His current research interests include physics of nanomaterials and device engineering for applications in biotechnology.

**Shao-Cheng Hsu** received the B.S. degree from National Chiao Tung University, Taiwan, in 2016, and the M.S. degree at New York University (NYU), New York, NY, USA, in 2018, both in electrical engineering. He is currently a senior engineer, working on the design of power management integrated circuits.

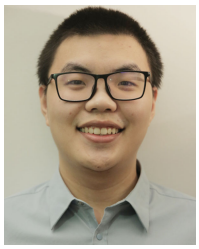

**Bohan Wu** (Student Member, IEEE) is currently working toward the B.S. degree in computer engineering at New York University (NYU), New York, NY, USA. He works as a Research Assistant at NYU Nano Lab. His current research interests include Data Analysis via Machine Learning and the design of Graphic User Interface (GUI) and its applications.

**Zhujun Huang** received the B.S. degree in electrical engineering from the Huazhong University of Science and Technology, Wuhan, China, and a M.S. degree in electrical and computer engineering from New York University (NYU), New York, USA in 2016 and 2018, respectively. She is currently working toward the Ph.D. degree in electrical and computer engineering at NYU. Her current research interest includes understanding the physics of nanomaterials for device applications.

**Xiaochang Pei** received the B.Eng. degree in electronic science and technology from Tianjin University, Tianjin, China, in 2018, and the M.S. degree in electrical engineering from New York University, New York, USA, in 2020. He is currently pursuing the Ph.D. degree in electrical engineering at the University of California, Irvine, CA, USA. His current research interests include micro- and nano-fabrication, biological sensors and devices, and microelectronic circuit design.

**Davood Shahrjerdi** (Senior Member, IEEE) received the Ph.D. degree in solid-state electronics from The University of Texas at Austin, Austin, TX, USA, in 2008. He was with the IBM Thomas J. Watson Research Center, Yorktown Heights, NY, USA until 2014. He is currently an Assistant Professor of Electrical and Computer Engineering at New York University (NYU), New York, NY, USA. His current research explores the science and technology of emerging nanomaterials and devices and their interfaces with silicon CMOS. Dr. Shahrjerdi was a recipient of the IBM Outstanding Technical Achievement Award and the IBM Master Inventor.